Technical Report: Battery Modeling and Performance Metrics

Anthongy Harris, Robert Cox, and Asis Nasipuri
Department of Electrical and Computer Engineering
University of North Carolina, Charlotte

1 Summary

This document focuses on the development of techniques for monitoring the performance of batteries as energy storage devices in low-power systems. Section 2 provides a brief review of battery operation and key metrics for monitoring battery performance in real systems. These metrics are termed key performance indicators (KPIs). Since equivalent electrical models are generally needed in performance monitoring applications, Section 3 reviews appropriate models. Section 4 then presents methods for using such models to determine the relevant KPIs. Section 5 compares different battery chemistries and presents an appropriate selection for low-power devices in light of the need to track the model parameters and KPIs presented previously. The remaining sections of this document focus on determining KPIs for the $\mathrm{LiFePO_4}$ cell chosen in Section 5. Other chemistries are briefly mentioned, however, as the techniques proposed here are general.

2 Battery Review

Batteries consist of series and parallel electrical combinations of individual cells such as the one shown in Fig. 1. These cells develop an electric potential through a series of electrochemical reactions. As shown in

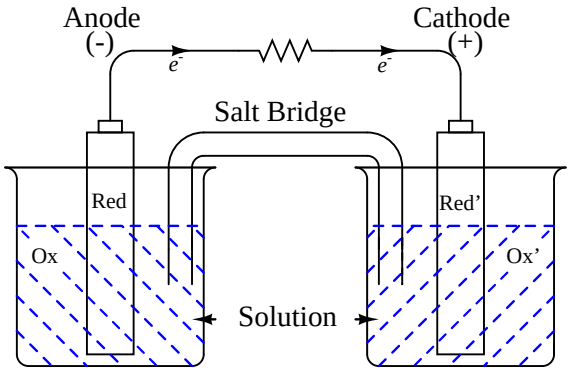

Figure 1: Typical electrochemical representation of a battery cell.

Fig. 1, the anode and cathode materials are known as reductants and are labeled as Red and Red', respectively. When placed in solution and connected as shown in Fig. 1, oxidation reactions occur at the anode and reduction reactions occur at the cathode. In the process of oxidation, the reductant material loses electrons, and in the process reduction, electrons are accepted by a material as an oxidant. At the anode, the resulting chemical reaction is expressed generally as

$$\mathrm{Red} \rightarrow \mathrm{Ox} + ne^{-}, \tag{1}$$

Note that the n electrons (e^{-}) flow into the electric circuit and the ionic oxidant material (Ox) is released into solution. At the cathode, the reaction is expressed as

$$\mathrm{Ox}' + ne^{-} \rightarrow \mathrm{Red}'. \tag{2}$$

as the electrons flowing into the cathode result in the release of an ionic oxidant material Ox′ into solution. Negative ions flowing between the two electrodes complete the circuit. The overall reaction performed in the circuit is expressed as the sum

$$\mathrm{Red} + \mathrm{Ox}' \rightarrow \mathrm{Red}' + \mathrm{Ox}. \tag{3}$$

and is known as a reduction-oxidation (redox) reaction.

As though all reactions take on the general form shown in Eq. 3, there exist two distinct types, namely those that can be reversed and those that cannot. Battery cells with irreversible redox reactions are referred to as primary batteries. Such devices are thus designed for only a single discharge cycle and can also be referred to as non-rechargeable. Cells capable of reversible redox reactions comprise what are known as secondary batteries. A reversal reaction can be initiated by applying an external electric potential across the battery terminals. The resulting reaction, which recharges the battery takes the form

$$\mathrm{Red}' + \mathrm{Ox} \rightarrow \mathrm{Red} + \mathrm{Ox}'. \tag{4}$$

Equations 3 and 4 are typically combined and written as

$$\mathrm{Red} + \mathrm{Ox}' \rightleftharpoons \mathrm{Red}' + \mathrm{Ox}. \tag{5}$$

Since the reactions described here are the driving forces behind battery operation any performance limitations can be traced back to the process of these reactions. Most importantly, a redox reaction can only drive a current through a circuit until all the Red and Ox′ elements have be appropriately converted to Ox and Red′ elements, respectively. Every battery thus has an initial charge which is usually given in units of A-hrs, and is known as the capacity. Another common quantity is the 1C or C-Rate. This value is the current required to fully discharge the battery in one hour. For example, a battery with a capacity of 2.85A-hrs has a 1C discharge rate equal to 2.85A. Similarly, a discharge rate of C/10 represents the constant current required to discharge the battery in 10 hours. This value is thus 285mA. In the case of secondary cells, there is a limit on the number of times that forward and reverse reactions can proceed before the chemical compounds begin to break down. This limit defines what is known as the cycle life.

2.1 Important Quantities

A set of key performance indicators (KPIs) have been designed to quantify the future performance and the current state of any battery regardless of its chemistry. The values of these KPIs depend upon various factors such as current, internal temperature, and ambient temperature. The three KPIs considered in this document are the following:

- State-of-Charge (SOC): The percentage of initial capacity available at a given instant in time
- End-of-Discharge (EOD): The time condition at which a battery is fully discharged. EOD is reached when the voltage drops to a predefined end-of-discharge voltage. The time until this occurs is denoted here as t_{EOD}.
- Remaining-Useful-Life (RUL): The time until a storage element is no longer useful.

Various techniques have been developed to measure or estimate the SOC of a given battery. The simplest method is Coulomb counting, and it requires one to measure the instantaneous terminal current $i(t)$. Assuming a constant initial capacity Q, then SOC can be determined as [7]

$$\mathrm{SOC}(t) = \frac{Q + \int_0^t i(\tau) d\tau}{Q}. \tag{6}$$

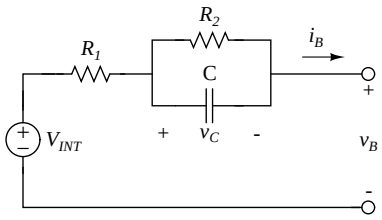

Figure 2: 1^{st} order RC lumped parameter model of a battery cell.

This methodology works well over short time intervals but it suffers from long-term drift issues caused by measurement error and changes in the initial capacity as a function of age, temperature, and other factors. The successful use of this technique requires frequent re-calibration. Although re-calibration is a possibility, the most successful techniques have been designed for high-power applications and have not been applied in low-power devices. More recently, researchers have proposed various state estimation schemes for differing battery chemistries. References [17, 3, 11] describe the various methodologies currently used in practice.

Although SOC is useful, one often wants to forecast the amount of time until a given battery is discharged and the time until a rechargeable cell is no longer useful. The quantity t_{EOD} is an estimate of the time until the SOC or the terminal voltage is lower than a predefined threshold. Calculation of this quantity takes into consideration the current SOC and the expected future current draw. Since t_{EOD} is based on a single discharge cycle, it is definable for both primary and secondary batteries. RUL, on the other hand, applies only for secondary batteries. Determination of this quantity is quite new, and most of the literature defines the RUL as the time until the full charge capacity has reduced to 80% of its initial value. Techniques for forecasting RUL and t_{EOD} are described in Section 4.

3 Equivalent Electric Battery Model

Many techniques used to estimate SOC, t_{EOD}, and RUL require the use of equivalent electric circuit models for the battery. Such models express the dynamic performance of the cell when under load. Various models have been used and the exact details of each depend upon the battery chemistry and the frequency range under consideration in the given application. Complete details are beyond the scope of this document and are presented in Refs. [8, 15].

To determine the impedance parameters of an equivalent circuit, a small-signal test current of the form

$$i(t) = I_o \sin \omega t \tag{7}$$

is applied to the battery and the resulting AC voltage is measured. If the frequency is varied over a range then one can generate a Nyquist plot showing the imaginary and real parts of the internal impedance as a function of frequency. An equivalent model can be generated to mimic the resulting frequency response. Such a methodology is known as electrical impedance spectroscopy (EIS) [14].

As noted above, various models can be used depending upon the frequency range of interest. In this document we focus upon short-term transients such as those initiated by a step change in current. An applicable model over this frequency range is the 1^{st} order RC network shown in Fig. 2. The response of this circuit is defined by the state equation

$$\frac{\mathrm{d}v_C}{\mathrm{d}t} = \frac{i_B}{C} - \frac{v_C}{R_2 C} \tag{8}$$

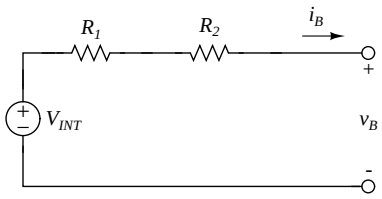

Figure 3: Resistive lumped parameter model of a battery cell.

and the measurement equation

$$v_B = V_{INT} - i_B R_1 - v_C. \tag{9}$$

Note that the values of the internal impedance parameters are functions of the state of health, temperature, and other factors. Depending upon the frequency range of interest and the battery chemistry under study, the model shown in Fig. 2 might be able to be simplified. For instance, it is shown later that the capacitive effect is strong for alkaline batteries and negligible in the case of LiFePO_4 cells. In the case of a weak capacitive effect, the circuit can be simplified as shown in Fig. 3. This simplification is important since it reduces measurement complexity. Furthermore, it is the values of the resistance R_1 and R_2 that are most typically sought in most monitoring applications. The reasoning for this is described in Sec. 4

4 Key Performance Indicators

Previously defined in Sec. 2, the KPIs in question for this document are the SOC, t_{EOD}, and RUL. Algorithms within literature range from the complex, chemically related state-space models with Kalman filters [19], to the simplistic, charge integration [7]. However, as such techniques exist a sufficient amount of resources are typically required as they are calculated through various simulation and estimation techniques, such as Monte Carlo (MC) simulations and particle filters (PFs) [21]. It is shown in literature that there exists a relationship between the internal impedance parameters to specific SOC and full charge capacity [22].

Through a different research effort, the internal resistance of a battery cell has been found to be relatable to the difference between the core temperature and that of the shell temperature. This relationship, between the core temperature and the measured resistance, is typically described by an Arrhenius function, i.e.

$$R = R_{ref} \exp \frac{T_{ref}}{T_c}, \tag{10}$$

where T_c and T_{ref} are the core and shell temperature of the battery cell, respectively and R_{ref} is a reference resistance at temperature T_{ref} [12, 18]. Core temperature is known to be relatively fluid in high-power applications such as PHEVs and HEVs, thus temperature control has been implemented in such applications [1]. Such temperature control, for low-power applications, has been deemed impractical. Furthermore, with current being of the scale of mA's, the internal heat generation is considered to be negligible. Therefore it is suggested that the variations in ambient temperature will become the dominant factor in the variability with respect to internal resistance along with age.

Prior to being able to track the desired KPIs, a methodology for obtaining the desired internal impedance parameters must be developed for low-power applications. It was discussed earlier that the ideal measurement process is accomplished through EIS. As effective as this methodology is, it is difficult to implement. To extract the impedance parameters in low-power applications, we use a time-domain approach described later in this document [4, 20].

Table 1: Secondary battery chemistry review

Type	Voltage	Energy Density	Efficiency	Cycle Life
	(V)	(Wh/kg)	(%)	(#)
NiMH	1.2	30-80	66%	500-1000
$LiFePO_4$	3.3	80-120	93.5%	8000+

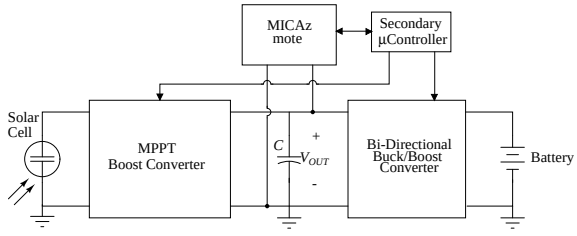

Figure 4: On-board power management system for individual nodes.

5 Powering Low-Power Applications

It is noted that the proposed power management system shown in Fig. 4 utilizes two separate energy storage devices that are supplied power through a photovoltaic cell. It is suggested that the energy storage devices be chosen in such a way as to maximize the use of the harvested energy. The energy storage devices in question must be capable of enduring low-frequency current pulses with a minimal pulse width and sustaining operation for years at a time. A super-capacitor and a secondary battery cell are thought to be the ideal choice. A super-capacitor is chosen due it is ability to endure the low-frequency current pulses with minimal pulse width. Where a secondary battery chemistry is chosen due its ability to store energy for prolonged periods of time. The power management system is designed to convert solar energy from the photovoltaic cell to that of the super-capacitor, when sufficient energy has been stored a bi-directional buck/boost converter is enabled to allow for maximum storage of the harvested energy. Adversely, as the previous control can only occur when daylight is available, an inverse process can occur at night. Such an inverse process only occurs if and only if the energy stored within the super-capacitor is below a minimal threshold.

With an understanding that there exists two distinct types of battery chemistries, primary and secondary, a series of battery chemistries are explored and a general overview can be viewed in Tbl. 1. As the power management system suggests, only secondary battery chemistries will be looked into, to allow for adequate storage of harvested energy. The desired battery chemistry will be chosen on the criterion of pursuing the maximum performance and longevity. Performance of a particular battery cell for the given topology will be dependent upon its ability to sustain an adequate OCV and an ability to undergo countless charge-discharge cycles. It should be noted that the chemistry chosen is anticipated to be placed under sub-optimal conditions. Such sub-optimal conditions can range from temperatures outside of its operational standards to an inability to fully charge due to a lack there of harvestable solar energy. Shown in Tbl. 1 the chosen batteries have been explored across various measurement terms. A discharge curve for their OCV across a single discharge can be seen in Fig. 5.

The suggested chemistries for such a power management system range from a nickel metal hydride (NiMH) cell to that of a new cell chemistry composed of lithium iron phosphate ($LiFePO_4$). In regards to a NiMH chemistry cell, homologous to that of alkaline cell, series and parallel combinations will be required as to produce a sufficient amount of electric potential. Noting that the nominal OCV for a single cell NiMH equates to 1.2V and trends with SOC as shown in Fig. 5. Furthermore, it has been shown that an average self-discharge occurs for NiMH battery cells at a linear rate of 1.5 percent per-day, leading to a full

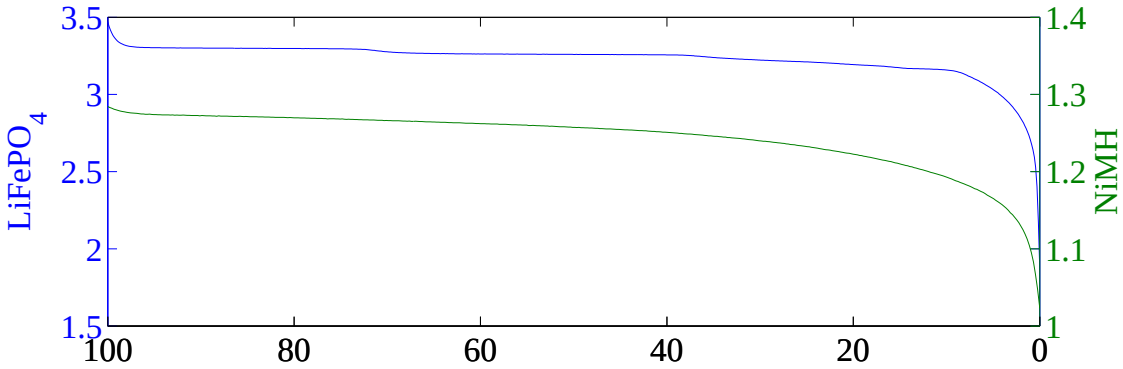

Figure 5: $LiFePO_4$ and NiMH secondary battery chemistries OCV with respect to SOC.

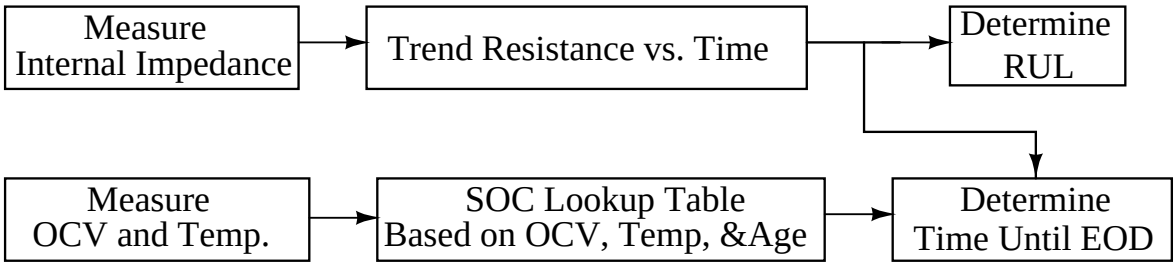

Figure 6: Proposed KPI measurement scheme for a low power application.

discharge with in roughly 65 days [5]. Along with an average cycle life of 500 charge-discharge cycles prior to an 80% of remaining charge capacity is reached. As NiMH have been found to have what is considered to be a low charge-discharge cycle life as well as a rapid self-discharge rate, a $LiFePO_4$ battery chemistry, however, is found to be of one that is capable of enduring a significant amount charge/discharge cycles while maintaining a low self-discharge rate. For example, allowing for a desired $LiFePO_4$ battery cell to be discharged and charged at a rate of 1C, an average cycle life has been found to be 8000+ cycles [2, 10, 6]. Furthermore, as observed in Fig. 5, a single cell can sustain an OCV greater than 2.7V until the last few percent of remaining SOC. Allowing for a singular cell to provide a sufficient amount of electric potential to power a particular node within the WMSN, thus reducing the overall cost of the system.

6 Developing a Robust Monitoring System

Figure 6 shows the monitoring scheme proposed for a rechargeable battery in a low power application. The sections below detail the different components of this process. Section 7 describes a method for measuring the impedance parameters of an operational battery. Section 8 explores the relationship between the internal resistance and the full charge capacity. Finally, Section 9 describes a process for determining the SOC without Coulomb counting as a process for determining t_{EOD}.

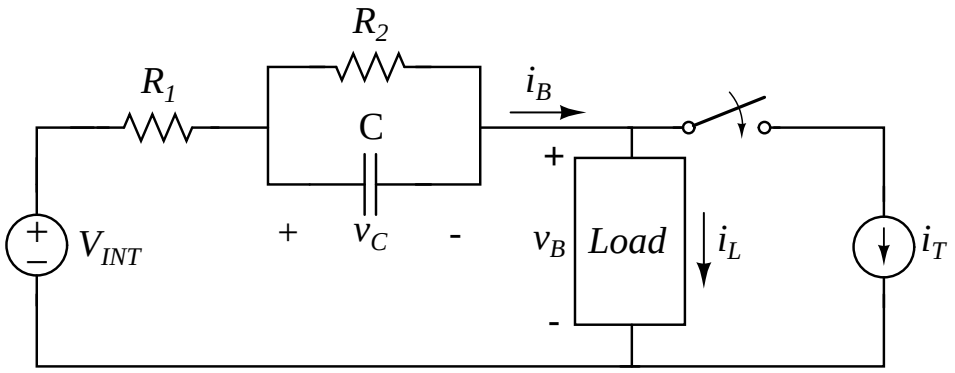

Figure 7: Equivalent electrical circuit for any low-power application with a pulse current source.

7 Estimating Internal Impedance

Figure 7 shows the scheme proposed for measuring the impedance parameters of a battery in a low power application. The battery is represented using the equivalent circuit presented in Fig. 3, and the sensor node is assumed to draw a load current $i_L(t)$. To measure the impedance parameters, a test source $i_T(t)$ is connected across the terminals. This source is designed such that it will draw an approximately constant current I_o for a time Δt,

$$i_T(t) = I_o u(t) - I_o u(t - \Delta t). \tag{11}$$

If i_L is assumed to be small, which is reasonable in a low power application, then it is possible to select $i_T(t)$ such that the terminal voltage during the pulse is

$$v_B(t) = v_B(0^-) - i_T(t)\left(R_1 + R_2 - R_2 e^{-t/(R_2 C)}\right), \tag{12}$$

where $v_B(0^-)$ is the terminal voltage measured immediately prior to connection of $i_T(t)$. Equation 12 can be reformulated in terms of a set of composite parameters as

$$v_B(t) = v_B(0^-) - i_T\left(\alpha - \beta e^{-t\gamma}\right), \tag{13}$$

where $\alpha = R_1 + R_2$, $\beta = R_2$, and $\gamma = 1/(R_2 C)$. Since $i_T(t)$ and $v_B(t)$ are both measurable, the unknown parameters can be determined by rearranging Eq. 13 so that all measured values are on one side of the equation. Since $v_B(0^-)$ must also be explicitly measured, we thus have

$$\frac{v_B(0^-) - v_B(t)}{i_T} = \alpha - \beta e^{-t\gamma}. \tag{14}$$

Figure 8 demonstrates the numeric procedure used to calculate the left side of Eq. 14. To estimate the values of α, β, and γ Eq. 14 is linearized. This process is performed in two steps. First, one takes the derivative of both sides yielding the relation

$$\frac{\partial}{\partial t}\left(\frac{v_B(0^-) - v_B(t)}{i_T}\right) = \gamma\beta e^{-t\gamma}. \tag{15}$$

Equation 15 is then linearized by computing the natural logarithm. On the right, one obtains

$$\ln(\gamma\beta e^{-t\gamma}) = \ln(\gamma\beta) - t\gamma, \tag{16}$$

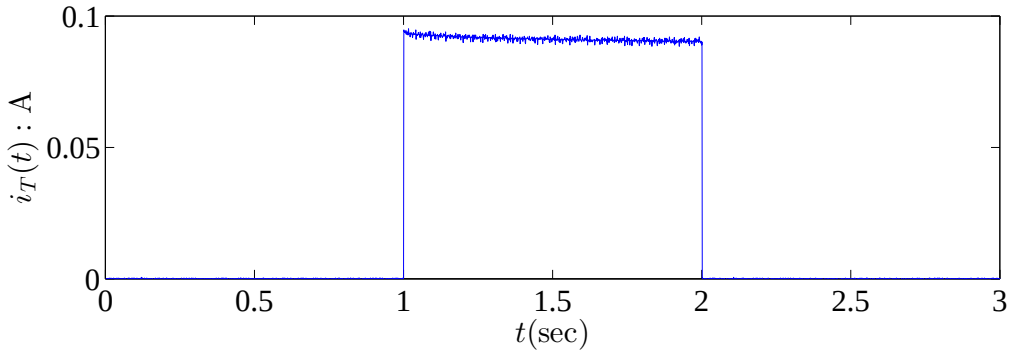

(a) Injection of test current, $I_o(t)$

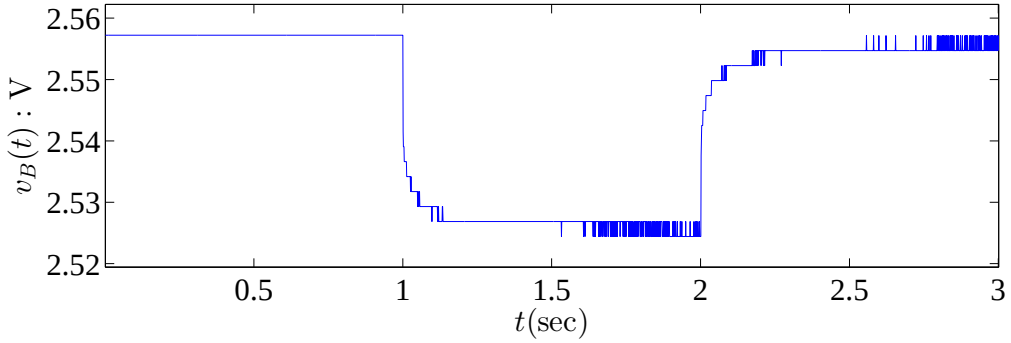

(b) Terminal voltage response, $v_B(t)$

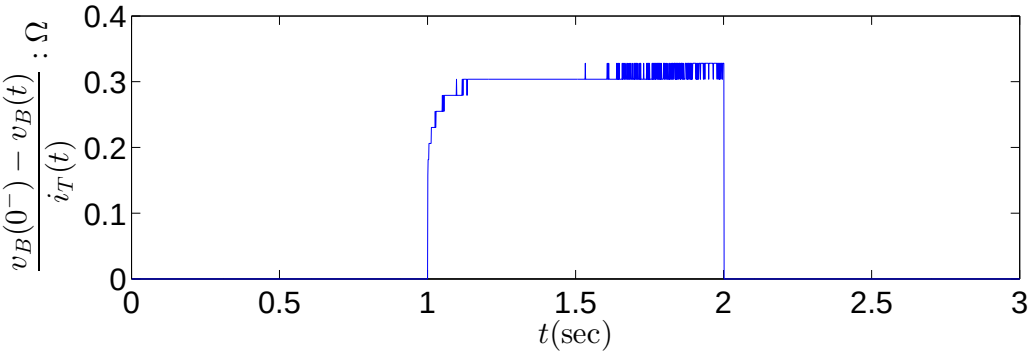

(c) Change in Voltage over load current

Figure 8: Measurable results from applying a step-wise pulse current, $I_o(t)$, to a non-rechargeable Alkaline battery

which is clearly linear with respect to time. Following the numeric derivative and the use of the natural logarithm, one obtains, a vector of values on the left hand side. For simplicity, we term this vector as $\kappa(t)$ and it has the form

$$\kappa(t) = \ln\left[\frac{\partial}{\partial t}\left(\frac{v_B(0^-) - v_B(t)}{i_T}\right)\right]. \tag{17}$$

To estimate the unknown parameters we use a least-squares approach. The problem is first reformulated in matrix form as

$$\underline{\kappa} = \underline{\underline{R}}\underline{\omega}. \tag{18}$$

assuming one has obtained k measurements at times $t_1, t_2, \ldots, t_k$, then the terms in Eq. 18 have the form.

$$\underline{\kappa} = \begin{bmatrix} \kappa(t_1) \\ \kappa(t_2) \\ \vdots \\ \kappa(t_k) \end{bmatrix}, \underline{\underline{R}} = \begin{bmatrix} 1 & t_1 \\ 1 & t_2 \\ \vdots & \vdots \\ 1 & t_k \end{bmatrix},$$

and

$$\underline{\omega} = \begin{bmatrix} \ln(\hat{\gamma}\hat{\beta}) \\ -\hat{\gamma} \end{bmatrix}$$

where $\hat{\gamma}$ and $\hat{\beta}$ are estimates of γ and β, respectively. The least-squares solution is thus

$$\underline{\omega} = \left(\underline{R}^T\underline{R}\right)^{-1}\underline{R}^T\underline{\kappa}. \tag{19}$$

The value of $\hat{\gamma}$ is clearly given by the second term in $\underline{\omega}$ which we denote as ω_2. Taking the exponential of the first term in $\underline{\omega}$ yields

$$\hat{\gamma}\hat{\beta} = e^{\omega_1}. \tag{20}$$

Rearranging, we have

$$\hat{\beta} = \frac{e^{\omega_1}}{\hat{\gamma}}. \tag{21}$$

Lastly, $\hat{\alpha}$ is solved for as the average between the summation of the newly found terms and that which was measured at time t_k taking on the form of

$$\hat{\alpha} = \frac{1}{K}\sum_{k=0}^{K}\left[\frac{v_B(0^-) - v_B(t_k)}{i_T(t_k)} + \hat{\beta}e^{-t_k\hat{\gamma}}\right]. \tag{22}$$

For verification purposes, the estimation process was carried out on the observed OCV and step-wise pulse current as described in Fig. 8. Resulting in the internal impedance parameters $R_1 = 0.166\Omega$, $R_2 = 0.117\Omega$, and $C = 0.383\text{F}$. Where plugging the estimated impedance parameters into Eq. 12, yields a minimal error across all time t, shown in Fig. 9.

The approach described above can be simplified in some limiting cases in order to improve the ability to perform the necessary operations on a low power node. For example, it was previously shown that some batteries have negligible dynamics when excited by a step current. If this is the case, the total resistance $R_1 + R_2$ can be found using the relation

$$R_1 + R_2 = \frac{\Delta v_B}{\Delta i_B}, \tag{23}$$

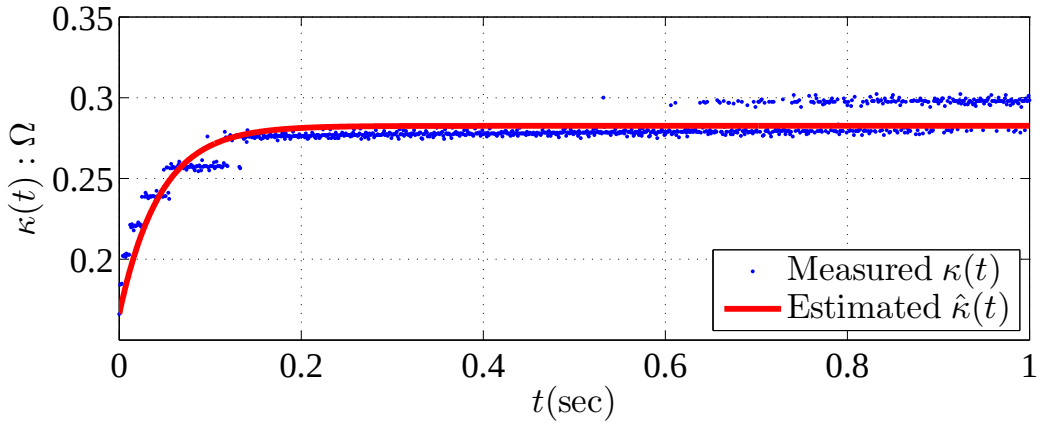

Figure 9: Using deterministic linear least squares, the unknown impedance parameters were found to be $R_1 = 0.166\Omega$, $R_2 = 0.117\Omega$, and $C = 0.383$F

where Δv_B is the change in voltage caused by a current step of magnitude Δi_B. Figure 10(a) and 10(b) demonstrate the applicability of this method using a $LiFePO_4$ battery. This method requires only two voltage and two current readings to be sampled and stored in memory. It is also possible to use this simplified approach on a battery with non-negligible dynamics. To do so, one must be sure to sample the voltage a fixed time after the start of the current pulse, so that the capacitive effects have subsided. Figure 10(c) and 10(d) show this applied to a alkaline cell. Note that this method is attractive because of its limited resource needs and is feasible since here resistances are the parameters of primary interest.

8 Remaining Useful Life

Documented techniques for RUL focus heavily on tracking internal resistance as a function of age. Algorithms in the literature tend to use non-linear state-estimators such as the PF which are far to computationally intensive for a low-power wireless node [23]. Furthermore, limited information is available in the literature with respect to the effect of temperature. This is likely due in part to the fact that battery temperature is often controlled in high power applications. To develop an effective, estimator for low power devices, it was decided to explore the effect of age and temperature on the resistance of a $LiFePO_4$ cell.

8.1 Tracking the Effect of Temperature

To understand the effect of temperature, a test battery was placed in a temperature chamber and discharged at low rates at typical ambient temperatures. In this case, the battery was discharged at a rate of C/50, and the resistance was measured every 5 minutes during the 50 hour test. Figure 11 shows the test circuit, which consists of two class A amplifiers. The amplifier on the left is designed to draw a continuous current $i_L(t)$, while the other acts as the excitation source. This second amplifier is controlled via an Arduino based microcontroller. If their total discharge rate is intended to be C/50, then the total charge removal in one hour is thus

$$\int_{1\text{Hour}} \frac{\text{C}}{50} dt = \int_{1\text{Hour}} i_L(t)dt + \int_{1\text{Hour}} i_T(t)dt. \tag{24}$$

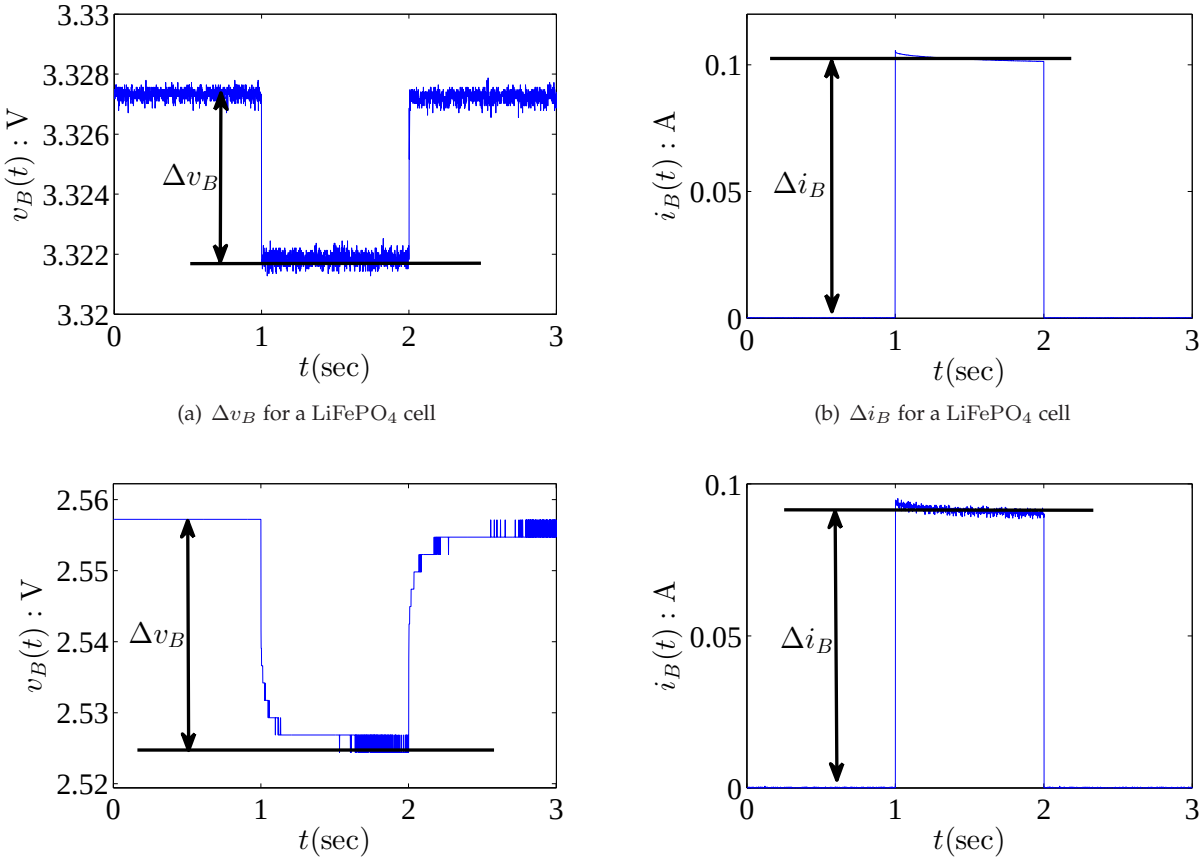

(a) Δv_B for a $LiFePO_4$ cell

(b) Δi_B for a $LiFePO_4$ cell

(c) Δv_B for an alkaline cell

(d) Δi_B for an alkaline cell

Figure 10: Determination of Δv_B and Δi_B for an alkaline and $LiFePO_4$ battery cell.

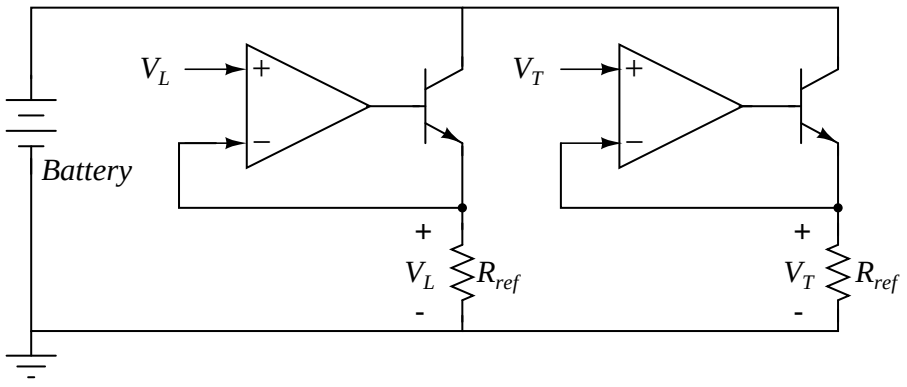

Figure 11: Amplifier circuit designed to measure the effect of ambient temperature.

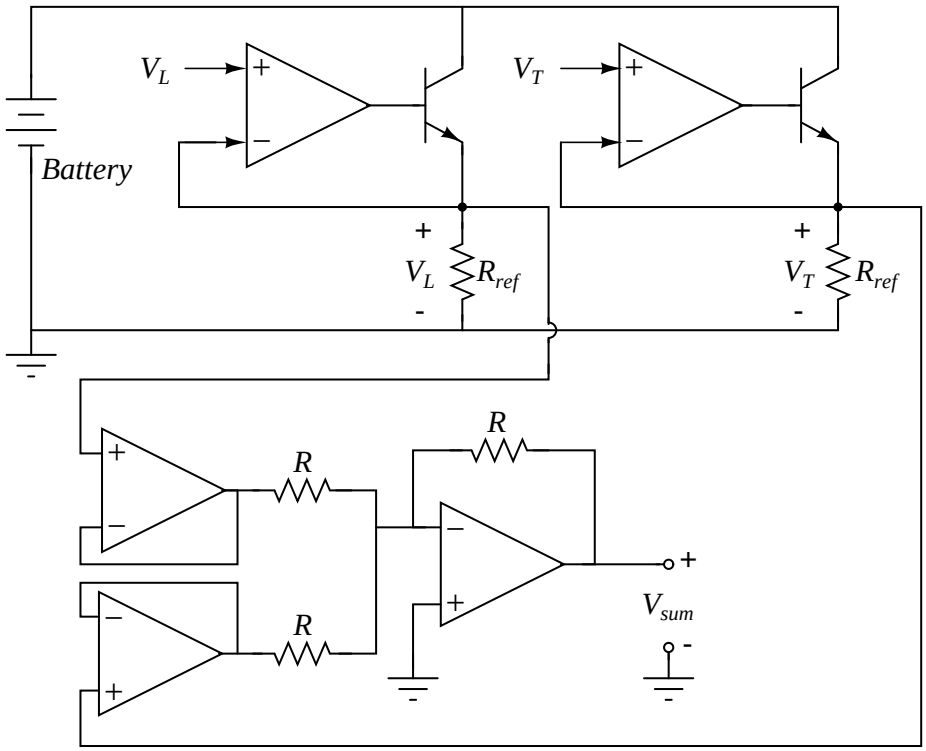

Figure 12: Amplifier circuit designed to measure the effect of ambient temperature with sampling points.

Assuming that the device draws n pulses of a height I_o and duration of Δt each hour, then Eq. 24 becomes

$$\int_{1\text{Hour}} (i_L(t) + i_T(t))dt = \int_{1\text{Hour}} \frac{\text{C}}{50} dt = I_o n \Delta t + \int_{1\text{Hour}} i_L(t)dt. \tag{25}$$

If i_L is a constant, then this is easily solved for the desired load current i_L. Note that both i_L and i_T are easily set in software using the voltage references V_L and V_T, which are provided by the Arduino.

During each discharge cycle the SOC is tracked through Coulomb counting. The total current is measured by the sensing circuit shown in Fig. 12. Note that an op-amp summer computes the total current, the op-amp is sampled by a Labjack UE9 DAQ system connected to a windows based PC. If the initial charge at $t = 0$ is Q, then the SOC at time t is

$$\text{SOC}(t) = \frac{Q - \int_0^t (i_L(\tau) + i_T(\tau))d\tau}{Q} \times 100\%. \tag{26}$$

If the sampling frequency f_s is sufficiently fast, then the integration in Eq. 26 can be approximated as the summation

$$\int_0^t (i_L(\tau) + i_T(\tau))d\tau \approx \frac{1}{f_s} \sum_{\tau_k=0}^{t} [i_L(\tau_k) + i_T(\tau_k)]. \tag{27}$$

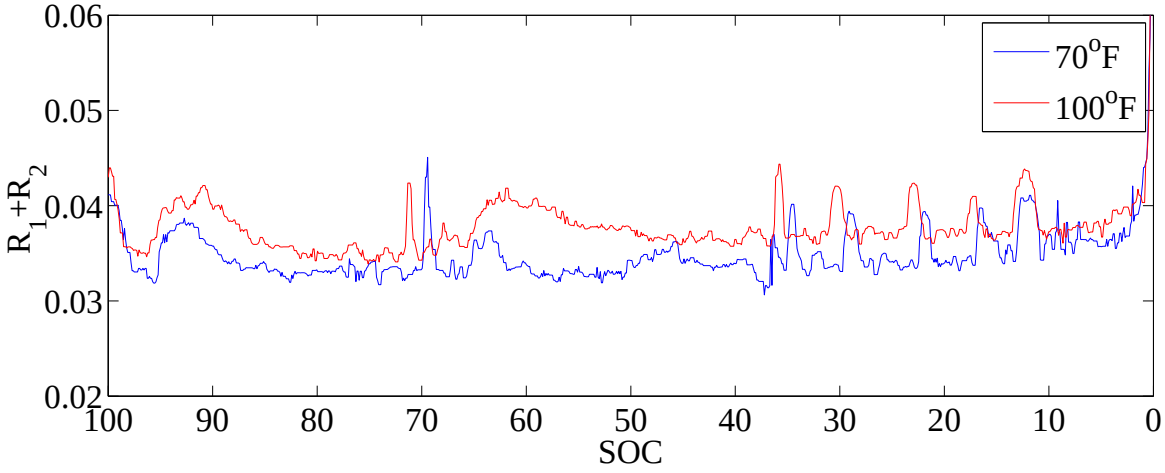

Figure 13: Internal resistance measurements of a $\mathrm{LiFePO_4}$ battery cell at 70 and 100 degrees Fahrenheit.

It should be noted that instrumentation layout is particularly crucial in this circuit since the change in voltage for a given current is relatively small and errors can easily occur. The internal resistance of a $\mathrm{LiFePO_4}$ cell was tracked at several different ambient temperatures using the aforementioned discharge set-up. Figure 13 shows some representative results over two different discharge cycles. From these results, one notices that the resistance does not change significantly over a single cycle and thus appears to be reasonably constant. Further note that the change if resistance with respect to temperature is relatively small with an average difference of about 3mΩ between 70 and 100 degrees Fahrenheit. Although by no means exhaustive, the data sets obtained during the course of this work are consistent with the relatively scant data available in the literature of $\mathrm{LiFePO_4}$ batteries [13]. The relatively small change in resistance do to temperature is encouraging as it suggests that such effects may potentially be negligible or viewed as unmodelled error terms when compared to the effect of aging. This effect is explored further in Sec. 8.3.

8.2 Tracking the Effect of Age

As a result of the chemical phenomena inside the battery, the internal resistance has been shown to increase approximately exponentially as a function of age alone [13]. If the initial resistance is R_o, then resistance over time is thus

$$R = R_o e^{\alpha t}, \tag{28}$$

where α is some unknown constant. Such a relationship is known as an Arrhenius function, and it is commonly used in aging studies and reliability analysis. Both the limited available literature and the published manufacturer data suggest that α is relatively small and growth is thus slow. As noted previously, for instance, the $\mathrm{LiFePO_4}$ battery has been shown to have a cycle life exceeding 8000 1C charge/discharge cycles [2, 10, 6]. To study the effect of age in a timely manner, an appropriate accelerated aging scheme had to be developed.

The accelerated aging test was performed using a circuit similar to that discussed in Sec. 8.1. Two class A amplifiers under the control of an Arduino microcontroller were again used. Figure 14 shows the circuit, which also includes a parallel connected charger. Once again, one of the amplifiers is used to inject a constant current, and the other is used to inject periodic pulses for resistance measurements. To accelerate the aging process, the current $i_L(t)$ was selected to be about 8C. For the battery under test, this equates to

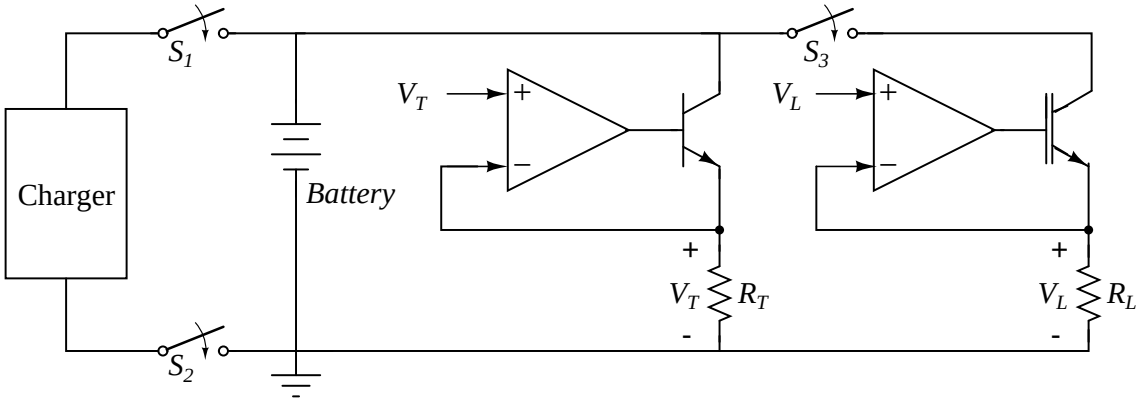

Figure 14: Amplifier circuit designed to measure the effect of aging.

an approximate 20A discharge current. This rate was selected because of hardware limitations. The current pulse used to measure resistance was 100mA for 1 second. An Arduino microcontroller used operates the charge/discharge hardware shown in Fig. 14. During each discharge, it opens S_1 and S_2 and closes S_3. A reference voltage V_L sets the discharge current. When the terminal voltage reads 2.0V, S_3 is opened and S_1 and S_2 are closed to recharge the cell. The discharge cycle is re-initiated based on the measured terminal voltage and temperature constraints.

Resistance was only measured at SOC=100% and SOC=25%. During initial testing, the battery surface temperature was found to rise some 20 degrees Celsius above room temperature, meaning that the core temperature was likely higher. In order to remove the effect of temperature, the battery was allowed to rest at zero current for a time t_r prior to each measurement. This time was selected based on measurements of the surface temperature. A complete block diagram for the aging process is shown in Fig. 15. Note that measurements were not recorded during every test in order to further accelerate the aging process (i.e. in order to perform more cycles per-day). Figure 16 shows results taken from nearly 1000 charge/discharge cycles. Note that the change in resistance has been normalized with respect to the initial measurement. Under the assumption that the exponential dependence on age is gradual, which appears to be the case, we chose to approximate Eq. 28 using a first-order Taylor series expansion. The resulting linear trend is shown in Fig. 16. The slow rise noted here is consistent with the available literature [2, 10]. Use of this information is explored in the next section. It should be noted, that roughly a 20 degree Fahrenheit difference in ambient temperature was observed throughout aging.

8.3 Developing an Estimator for RUL

As previously stated, the internal resistance of a battery as a function of age alone can be modelled using the Arrhenius function described by Eq. 28. Both the data presented in the previous section and the recent literature on $LiFePO_4$ batteries suggest that α is considerably small and that a first-order Taylor series approximation is reasonable. Figure 16 shows that temperature fluctuations, measurement errors and other effects clearly cause variations within the data. Given that such fluctuations are expected in the field, some form of compensation is needed. Thus we suggest the use of a Kalman filter [25], which assumes that the

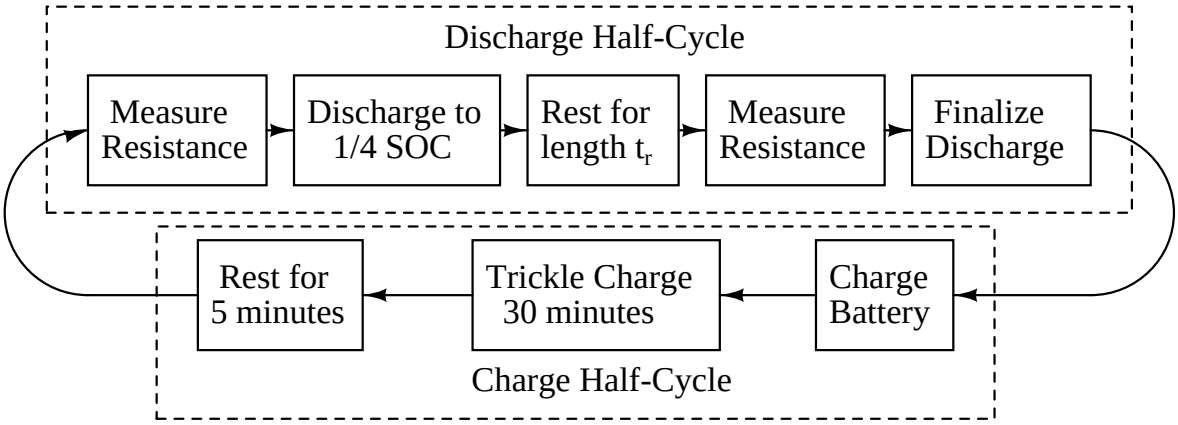

Figure 15: Block diagram of the aging charge/discharge process.

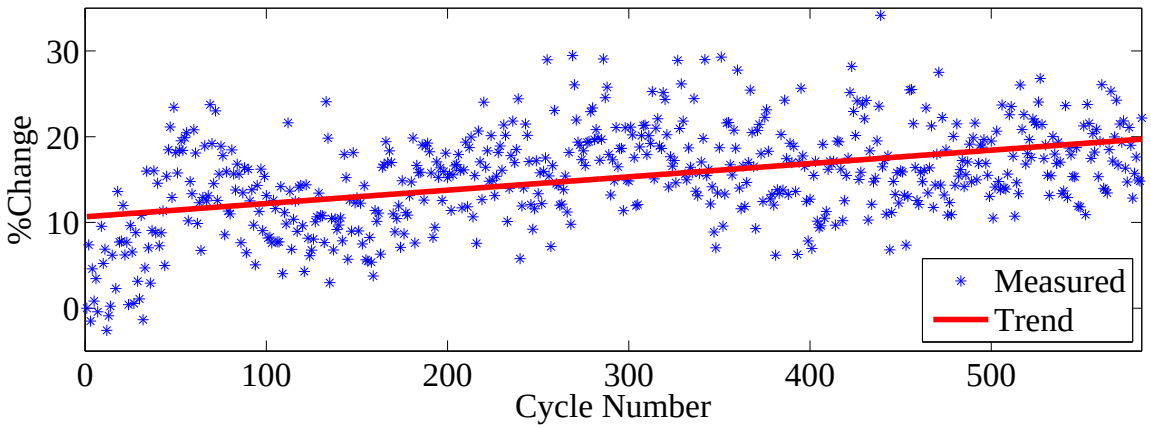

Figure 16: Measured %Change of internal resistance versus cycle number.

resistance is a state variable that varies slowly over time. In general, the state transition relations are

$$x_k = \Phi x_{k-1} + \mathcal{N}(0, S_k), \tag{29}$$

and the measurement relationship is

$$z_k = H x_k + \mathcal{N}(0, R_k). \tag{30}$$

In this case x_k is simply the true normalized resistance at time t_k and we assume that any change between adjacent time steps is simply cause by zero-mean normally distributed noise of variance S_k. Such noise is intended to capture the effect of temperature and other unmodelled factors. Similarly the noise-corrupted measurement z_k are the resistance values obtained by our measurement system. These are certainly noise-corrupted, and we view the noise to be zero-mean white-noise process of variance R_k. Although Φ and H are simply unity in this case, we proceed more generally and allow them to remain as variables.

Predictions based on the Kalman filter proceeds in several steps. First, one pre-estimates the normalized resistance at time t_k prior to the arrival of any new measurements. This value is denoted as $x_k(-)$ and it is represented as

$$\hat{x}_k(-) = \Phi \hat{x}_{k-1}(+). \tag{31}$$

where $\hat{x}_{k-1}(+)$ is the estimates normalized resistance at time t_{k-1}. Once this value is computed, the corresponding error covariance is calculated. It is

$$P_k(-) = \Phi P_{k-1}(+) \Phi^T + S_k \tag{32}$$

where $P_{k-1}(+)$ is the error covariance at time t_{k-1}. Once a measurement has been obtained, it is used to implement the resistance post-estimate according to the relation

$$\hat{x}_k(+) = \hat{x}_k(-) + K_k(Z_k + H\hat{x}_k(-)). \tag{33}$$

Note that the gain matrix K_k is given by

$$K_k = P_k(-) H^T \left[H P_k(-) H^T + R_k \right]^{-1}. \tag{34}$$

Lastly, the error covariance for the final estimate is computed using the relation

$$P_k(+) = \left[I + k_k H \right] P_k(-). \tag{35}$$

The process then returns to Eq. 31 and repeats. This recursive algorithm should smooth the resistance data over time.

The proposed algorithm was applied to the data shown in Fig. 16. The variances R_k and S_k were arbitrarily selected to be 5.4 and 0.0024, respectively. The relatively large value of R_k belies the fact that even small measurement errors can cause relatively large changes in measured resistance. This is simply a result of the relatively small changes in voltage caused by the 100mA pulses. Conversely, the small value of S_k reflects the confidence in the system model. The initial guess for the normalized resistance was 0 with a large error covariance (i.e. $R_o(+) = 1000$). Figure 17 shows the smoothed output and the original data. Note that a clear upward trend is observed. From an implementation perspective, the proposed algorithm is relatively easy to implement in a low-power device. Each step within the algorithm is designed to be completed within four to eight clock cycles depending upon whether or not the desired variable must be stored or loaded from RAM.

Although not exhaustive, the trends observed here are consistent with other published studies [10, 6]. Ultimately, it might be possible to correlate the resistance with capacity as in [21]. For a battery with such a long cycle life, such testing would take considerable time. It is likely that a reasonably accurate measurement of the resistance would be sufficient to track the age and state-of-health of the battery. Such information would likely be useful in low-power applications, where very little health management is currently available. It should be noted that the battery used here lost roughly 14% of its initial capacity during these experiments.

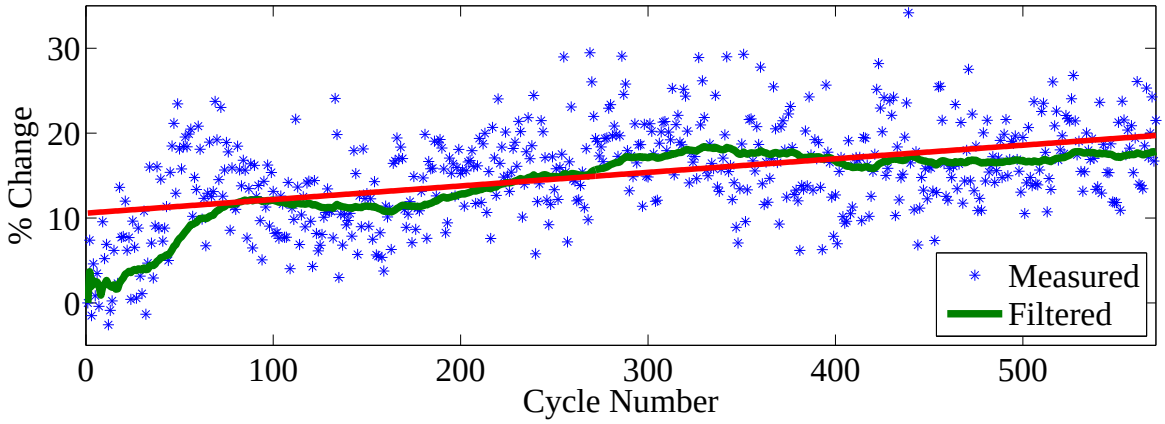

Figure 17: Filtered %Change of resistance utilizing a Kalman filter.

Table 2: Defined Parameters [16]

Var	Values	Var	Values	Var	Values	Var	Values
I_{Bt}	20 mA	T_{Bt}	140 ms	I_{Br}	20 mA	T_{Br}	140 ms
I_{Dt}	20 mA	T_{Dt}	140 ms	I_{Dr}	20 mA	T_{Dr}	140 ms
I_P	8 mA	T_P	3 ms	I_S	7.5 mA	T_S	112 ms

9 End-of-Discharge

To help sustain a network of low-power nodes it, powerful modern algorithms have been developed for this purpose claiming accuracies better than 1% [24]. The approaches are designed for a much higher power application than those considered here. These algorithms are based on look-up tables that provide expected open-circuit voltages for a given temperature.

In this case, the typical load current is on the order of several mA and the resistance is tens of m$Omega$'s, thus the voltage drop across the internal resistance is negligible and one is essentially always measuring the open-circuit voltage. Given a look-up table for open-circuit voltage as a function of temperature, one could detect the SOC. At any given time t, the remaining charge stored in the battery is

$$Q_{rm} = Q_{max}(\mathrm{SOC}(t) - \mathrm{SOC}_L) \tag{36}$$

where SOC_L is a predefined minimum operational threshold and SOC(t) is the value pulled from the table at time t. Given measurements of the devices current i_{avg}, one could calculate

$$t_{EOD} = \frac{Q_{rm}}{i_{avg}}. \tag{37}$$

Where, i_{avg} could be estimated using the approximation [16]

$$i_{avg} = \frac{I_{Bt}T_{Bt}}{T_B} + I_{Dt}T_{Dt}M + N\frac{I_{Br}T_{Br}}{T_B} + I_{Dr}T_{Dr}O + I_{Dt}T_{Dt}F + \frac{I_sT_s}{T_D} + N_PI_PT_P. \tag{38}$$

Noting that I_x and T_x are the average current and duration periods for a given operation, a table with respective values has been generated and can be observed in Tbl. 2 [16].

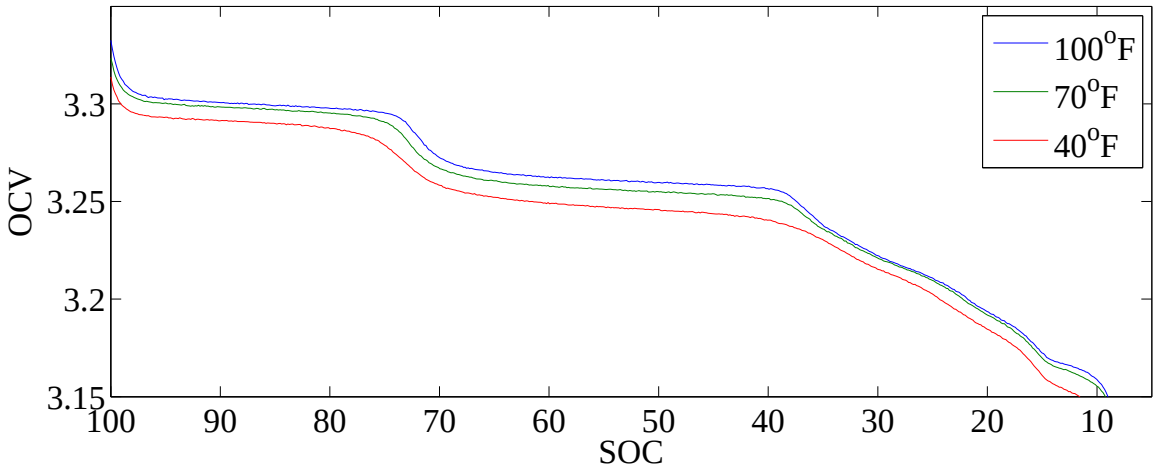

Figure 18: Correlating OCV of a $LiFePO_4$ cell to specific SOC at various ambient temperatures.

Some initial data was collected for the look up table, from an example $LiFePO_4$ battery. Fig. 18 shows example curves recorded at C/50 at different temperatures. Some further data collection is required in order to complete this table. Data collection was unfortunately stopped due to an equipment failure caused by another party on a different project. Figure 19 shows a potential useful observation. Note that the slope of the OCV verse SOC curve changes at certain predefined points, with little effect from temperature. This observation has been noted by other researchers and is seen as a possible means for calibration [6, 9].

References

[1] Nissan leaf electric car. Online, 2013.

[2] INC. A123 Systems. An overview of the structure, properties and benefits of a123 systems proprietary lithium ion battery technology. Technical report, A123, 2008.

[3] Mohammad Charkhgard and Mohammad Farrokhi. State-of-charge estimation for lithium-ion batteries using neural networks and ekf. *Industrial Electronics, IEEE Transactions on*, 57(12):4178–4187, 2010.

[4] Martin Coleman, William Gerard Hurley, and Chin Kwan Lee. An improved battery characterization method using a two-pulse load test. *Energy Conversion, IEEE Transactions on*, 23(2):708–713, 2008.

[5] John K Erbacher. Nickel-metal hydride battery technology evaluation. Technical report, DTIC Document, 1996.

[6] Jens Groot. *State-of-health estimation of Li-ion batteries: cycle life test methods*. PhD thesis, Chalmers University of Technology, Göteborg, 2012.

[7] Terry Hansen and Chia-Jiu Wang. Support vector based battery state of charge estimator. *Journal of Power Sources*, 141(2):351–358, 2005.

[8] Richard Lee Hartmann. *An aging model for lithium-ion cells*. PhD thesis, University of Akron, 2008.

[9] Robert A. Huggins. *Advanced Batterues: Materials Science Aspects*. Springer, 2009.

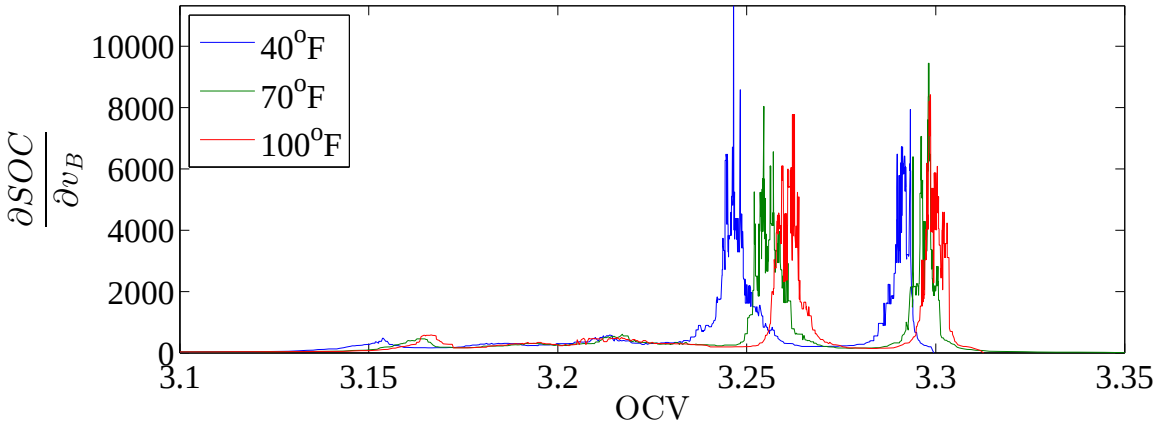

Figure 19: Change is SOC with respect to OCV for a $\mathrm{LiFePO_4}$ battery cell at various ambient temperatures.

[10] Thomas D Hund and David Ingersoll. Selected test results from the lifebatt iron phosphate li-ion battery. Technical report, Sandia National Laboratories, 2008.

[11] Il-Song Kim. The novel state of charge estimation method for lithium battery using sliding mode observer. *Journal of Power Sources*, 163(1):584–590, 2006.

[12] Xinfan Lin, Hector E Perez, Jason B Siegel, Anna G Stefanopoulou, Yi Ding, and Matthew P Castanier. Parameterization and observability analysis of scalable battery clusters for onboard thermal management. Technical report, DTIC Document, 2011.

[13] Xinfan Lin, Hector E Perez, Jason B Siegel, Anna G Stefanopoulou, Yonghua Li, R Dyche Anderson, Yi Ding, and Matthew P Castanier. Online parameterization of lumped thermal dynamics in cylindrical lithium ion batteries for core temperature estimation and health monitoring. *IEEE Transactions on Control Systems Technology*, 21(5):1745–1755, 2012.

[14] J Ross Macdonald. Impedance spectroscopy. *Annals of biomedical engineering*, 20(3):289–305, 1992.

[15] Lalit P Mandal and Robert W Cox. A transient-based approach to estimation of the electrical parameters of a lead-acid battery model. In *Energy Conversion Congress and Exposition (ECCE), 2010 IEE*, pages 4238–4242, 2010.

[16] Amitangshu Pal, Bonee Soibam, and Asis Nasipuri. A distributed power control and routing scheme for rechargeable sensor networks. In *Southeastcon, 2013 Proceedings of IEEE*, pages 1–5. IEEE, 2013.

[17] Shuo Pang, Jay Farrell, Jie Du, and Matthew Barth. Battery state-of-charge estimation. In *American Control Conference, 2001. Proceedings of the 2001*, volume 2, pages 1644–1649. IEEE, 2001.

[18] Hector E Perez, Jason B Siegel, Xinfan Lin, AAnna G Stefanopoulou, Yi Ding, and Matthew P Castanier. Parameterization and validation of an integrated electro-therma cylindrical lfp battery model. In *JSME 2012 11th Motion and Vibration Conference*, 2012.

[19] Gregory L Plett. Extended kalman filtering for battery management systems of lipb-based hev battery packs: Part 2. modeling and identification. *Journal of power sources*, 134(2):262–276, 2004.

[20] Amir Hossein Ranjbar, Anahita Banaei, Amir Khoobroo, and Babak Fahimi. Online estimation of state of charge in li-ion batteries using impulse response concept. *Smart Grid, IEEE Transactions on*, 3(1):360–367, 2013.

[21] Bhaskar Saha and Kai Goebel. Uncertainty management for diagnostics and prognostics of batteries using bayesian techniques. In *Aerospace Conference, 2008 IEE*, pages 1–8. IEEE, 2008.

[22] Bhaskar Saha, Kai Goebel, Scott Poll, and Jon Christophersen. Prognostics methods for battery health monitoring using a bayesian framework. *Instrumentation and Measurement, IEEE Transactions on*, 58(2):291–296, 2009.

[23] Bhaskar Saha, Edwin Koshimoto, Cuong C Quach, Edward F Hogge, Thomas H Strom, Boyd L Hill, Sixto L Vazquez, and Kai Goebel. Battery health management system for electric uavs. In *Aerospace Conference, 2011 IEEE*, pages 1–9. IEEE, 2011.

[24] Michael Vega. *Single-Cell Impedance Track Gas Gauge for Novices*. Texas Instruments, slua422 edition, June 2007.

[25] Greg Welch and Gary Bishop. An introduction to the kalman filter. Technical report, University of North Carolina at Chapil Hill, 1995.